Proceedings of ASME Turbo Expo 2021
Turbomachinery Technical Conference and Exposition
GT2021
June 7-11, 2021, Virtual, Online

GT2021-59111

AERO-THERMAL CHARACTERIZATION OF ACCELERATING AND DIFFUSING PASSAGES DOWNSTREAM OF ROTATING DETONATION COMBUSTORS

James Braun
Purdue University
West Lafayette, IN

Guillermo Paniagua
Purdue University
West Lafayette, IN

Donald Ferguson
National Energy Technology Laboratory
Morgantown, WV

ABSTRACT

Cycle benefits of rotating detonation engines show up to five percentage points of efficiency gain for low-pressure ratio engines. An optimal integration between the combustor and the turbine needs to be guaranteed to realize this potential gain. The rotating detonation combustor (RDC) exhausts transonic flow with shocks rotating at frequencies ranging from a few to tens of kilohertz depending on the number of present waves. Hence, the turbine design requires precise knowledge of the fluctuations and losses downstream of the combustor. This paper focuses on the quantification of fluctuations and losses for accelerating and diffusing passages. The analysis of the combustor is performed via reactive unsteady Reynolds Averaged Navier-Stokes (URANS) simulations. The unsteady RANS equations are solved via CFD++ from Metacomp with a one-step reaction mechanism for an H_2-air mixture. The resolving of the boundary layer is achieved with a structured mesh of around 36 million cells. Inlet pressure of 10 bar and two different back pressures are applied to the combustor to model the interconnection with downstream turbines. Finally, we present and assess a methodology to reduce the computational time to model these passages ten times.

Keywords: Rotating detonation engines

NOMENCLATURE

α [deg]	Flow angle
A [m^2]	Area
ρ [kg/m^3]	Density
M [-]	Mach number
$\dot{m}$ [kg/s]	mass flow
H_{total} [J]	Total enthalpy
T]K]	Temperature
t [s]	Time
U_{axial} [m/s]	Axial velocity
p [Pa]	Pressure
γ [-]	Heat capacity ratio
z [m]	axial coordinate

SUBSCRIPTS

0	Total condition
STD	Standard deviation
s	Static

1. INTRODUCTION

Pressure gain combustion could offer significant efficiency benefits for future power generation [1]. However, the pressure gain achieved within a rotating detonation combustor (RDC) is encompassed with supersonic rotating shock waves at the combustor exhaust, featuring large fluctuations of pressure, temperature, and flow velocity [2]. In the past decade, significant efforts have been attributed to the understanding of combustors, and an extensive review of the operation of rotating detonation combustors has been performed by Anand et al. [3] and Ma et al.[4]. Modeling of such combustors has been performed with two-dimensional Euler solvers [5], three-dimensional Reynolds-averaged Navier-Stokes solvers [6] with induction parameter models, one-step and multi-step reaction mechanisms [7]. More recently, Pal et al. [8] modeled the AFRL RDC with air-ethylene through Large Eddy Simulations (LES) and a 21 species, 38 reactions reaction mechanism. Sato et al. [9] performed high fidelity simulations through an OpenFoam solver for a hydrogen-air mixture with 19 reactions and 9 species. Direct quantification of the pressure gain requires a measure of total pressure of the flow in the exhaust which was recently performed by Bach et al for an unrestricted RDC [6], However due to extreme temperatures in the exhaust that make it difficult to achieve an accurate measure of total pressure, an alternative method utilizing equivalent available pressure has been proposed with the assumption of choked back-pressured RDCs [10]. During the past years, several concepts have been proposed to extract power from RDCs. For supersonic exit flows, axial supersonic turbines [11], bladeless ideas [12] or radial outflow turbines can be employed [13]. Asli et al. [14] quantified the damping and losses across several NACA profiles at the exhaust of an RDC with flow angle reduction of up to 57%. Little information is available on the optimal design of diffusing passages between combustor and turbine. For steady flows, boundary layer methods have been developed to predict flow separation in diffusers [15]. Dean and Senoo [16] found that upstream rotating wakes influence the diffuser passages; this behavior is a function of the geometry and instability amplitude. Specifically, three objectives are outlined after the solver validation and description. The first objective is to assess the fluctuations (i), heat load (ii) and losses (iii) occurring within the

coupled combustor and downstream passage. The different investigated geometries are described (section 3.1), followed by the characteristics in an accelerating passage for supersonic turbines (section 3.2), in a diffusing passage for subsonic turbines[17] (section 3.3) and overall total pressure losses (section 3.4). These outcomes can then be used as input conditions for turbine designers. The second objective is to analyze the influence of the downstream passage (accelerating or diffusing) on the combustor performance (section 4.1) and isolated downstream passage losses (4.2). The third objective is to determine a strategy to investigate diffusers at a reduced computational cost for future optimization of diffusing elements (section 4.3) and integration within combustor design tools [18].

2. Methodology

2.1 Solver description

The analysis of the combustor is performed via reactive unsteady Reynolds Averaged Navier-Stokes (URANS) simulations. The URANS equations are solved via CFD++ from Metacomp [19] with a one-step reaction mechanism for stoichiometric H_2-air [6]. An in-depth comparison with other detailed reaction schemes is provided in the appendix (A4). Limitations on the one-step reaction mechanism include reduced performance at handling for rich mixtures[20]. The turbulence closure is provided by the k-omega SST model. The solver is a finite-volume density based solver. Convective fluxes were solved through the Harten-Lax-Van Leer contact approximate Riemann Scheme and a second Order Total Variation Diminishing (TVD) polynomial interpolation was selected with a continuous limiter. Implicit time-integration with fixed a global timestep of 0.1 μs and an internal iteration termination criterion of 0.1 which is, an essential parameter for unsteady flows [21]. Time step and grid spacing were selected based on [22] for grid independence.

2.2 SOLVER VALIDATION

Readily available experimental data of the Purdue Turbine High-Pressure Optical RDE platform [23] is used for the solver validation. Other RDCs employing axial inflow for oxidizer for engine integration purposes, such as described by Chacon et al. [24] and Stechmann et al. [25], have successfully used similar flow injection schemes. The selected operating condition has an inlet mass oxidizer mass flux of 750 kg/m^2/s and the temperature of oxidizer and fuel are 290K and equivalence ratio of one. The outer diameter of the combustor is 0.068m and the inner radius upstream of the expansion is 0.057m with an axial length of 0.1m. The outlet-to-inlet area ratio from downstream of the backward-facing step to the outlet is 1.6 (corresponding to an A/A* of Mach 1.9 for a γ of 1.28) and further details on the geometry are found in [23]. Figure 1a shows the RDC test setup with four oxidizer feed tubes feeding into the air manifold, a metal diverging center body, and a quartz window with full optical access across the injection and combustion region. High-frequency imaging of the exit plume, revealed a single detonation wave traveling at approx. 4.3 kHz for a wide range of operating conditions with a non-preheated H_2-air mixture [23]. The numerical domain of this non-premixed combustor is visualized in Figure 1b in which fuel and air plenum were modeled as total inlet and total pressure boundary conditions. The outlet static pressure was set to one bar. ICEM was used to generate a structured grid, more specifically, one sector (3.6 degrees) was meshed and rotated to obtain the full geometry. The total mesh count was around 48M cells and a snapshot of mesh in the injection region is visualized in Figure 1c.

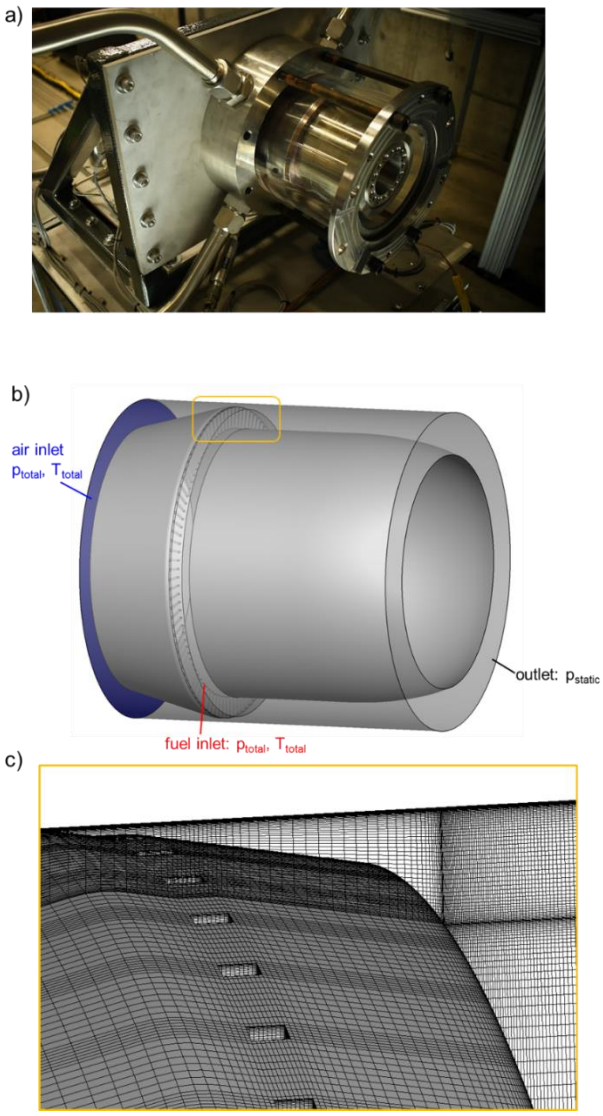

Figure 1 a) experimental setup [17] b) numerical model of the non-premixed simulation, b) mesh refinement near the fuel injector.

A one wave solution was predicted by the URANS simulations and the cycle frequency of the simulations was overpredicted by 10% with the experiments and within error bounds of other published CFD comparisons with experiments[9] Figure 2a depicts a snapshot of a one MHz chemiluminescence image[23] with several identified zones; a combustion zone covering the entire radial height (A), a partial combustion zone (B), and a

reflected shock (C). The temperature contour taken at the inner and outer end wall from the URANS simulations predicts the same trends (Figure 2b), with a primary combustion region (A), partial combustion region (B1, pointing to the detonation wave signature on the outer end wall, and B2 pointing to the lower end wall with a leading shock traveling through the burnt products), and a reflected shock (C).

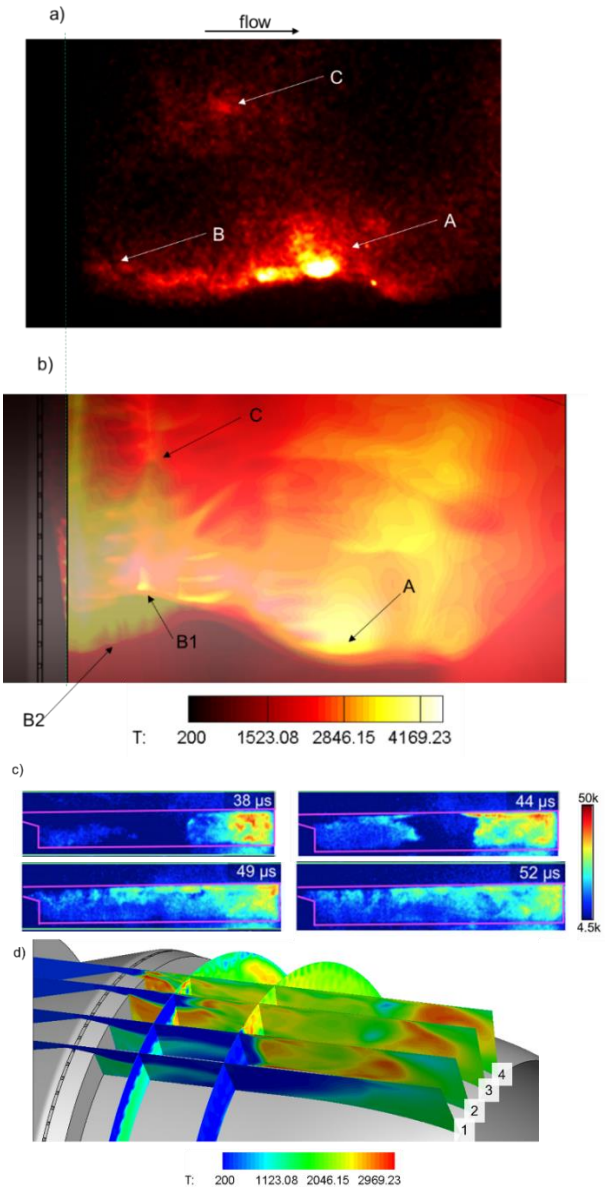

Figure 2 a) snapshot of the detonation wave through MHz chemiluminescence [23]*, b) temperature field of the inner and outer endwall through 3D URANS, c) 1 MHz OH-PLIF at a constant tangential location* [26]*, d) four cuts at constant tangential location through 3D URANS*

Via 1 MHz OH-PLIF[26] (Figure 2c) different snapshots of the refill regime as a function of the radial height are highlighted. Before the detonation wave arrival, at 38 µs, the fresh air-fuel mixture fills most of the plenum while the region right downstream of the backwards facing step is filled with remaining combusted products. Upon the arrival of the detonation wave (44 µs), the downstream shock leads, and all mixture is combusted at timestep t=49 µs. Figure 2d depicts the temperature field predicted by the URANS simulations at four constant angular positions. Plane one contains the fresh combustibles covering 75% of the axial length prior to detonation wave arrival, plane two upon arrival of the detonation wave with the downstream leading shock ("A" in Figure 2c, plane 3: in which all fresh mixture has ignited but a section of unburnt products appears near the injection plane and plane 4 with complete combustion of the products. Computational time was 840 hours on 14 10-core Intel Xeon-E5 processors.

2.3 Reduced numerical domain for downstream component analysis

Figure 3a depicts a reduced numerical domain for which the RDC inlet is modeled as an inlet total pressure and inlet total temperature plenum (inlet total temperature is kept constant at 270K). The outlet is set as mixed supersonic-subsonic or as fixed backpressure. Injection area and combustor geometry are modeled according to section 2.4. Figure 3b depicts the mesh near the injection and backward-facing step. The mesh consists of hexahedral structured elements (via Ansys ICEM), with around 36 million cells. The non-dimensional first layer thickness, y+, was kept below one within the downstream investigated passage. This reduced method decreases mesh count by 25%, with consequent CPU cost reduction and enabling to analyze multiple combustor passages.

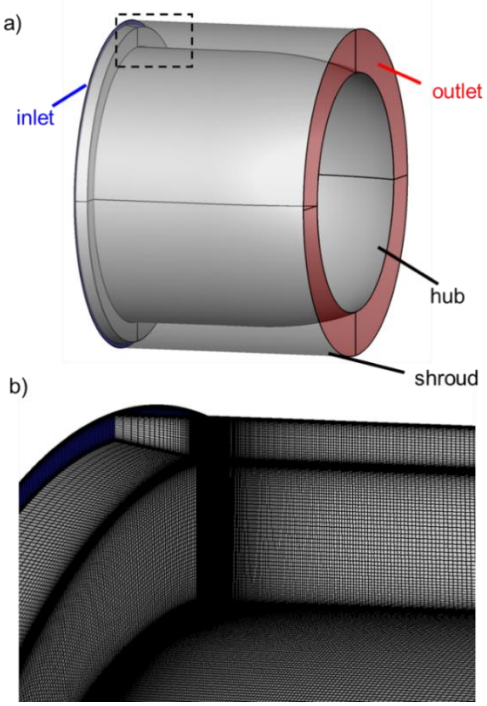

Figure 3 a) Computational domain of the premixed rotating detonation combustor (RDC), b) structured mesh visualization on the hub and tangential cut in the selected region of (a)

The RDC flow field is displayed in Figure 4 for an inlet total pressure of five bar and atmospheric backpressure, totaling a mass flow of around 0.8 kg/s. Downstream of the backward-facing step, a fresh mixture (blue region) zone is cyclically consumed by the detonation wave traveling at 4.6 kHz. Directly downstream of the backward-facing step, old combustion products from the previous cycle exist with a significant circumferential velocity and interact in the form of a shear layer with the axially injected expanding high-speed fresh reactants (highlighted in "A" in the tangential slice in Figure 4), with similar flow features to the non-premixed case. Further downstream (~0.06m, "B" in Figure 4), the fresh mixture of H_2-air consumes the combustor's entire height (region B). A comparison to the non-premixed simulations is provided in the appendix A3. Additionally, the effects of viscous versus non-viscous wall modeling is provided in Appendix A5.

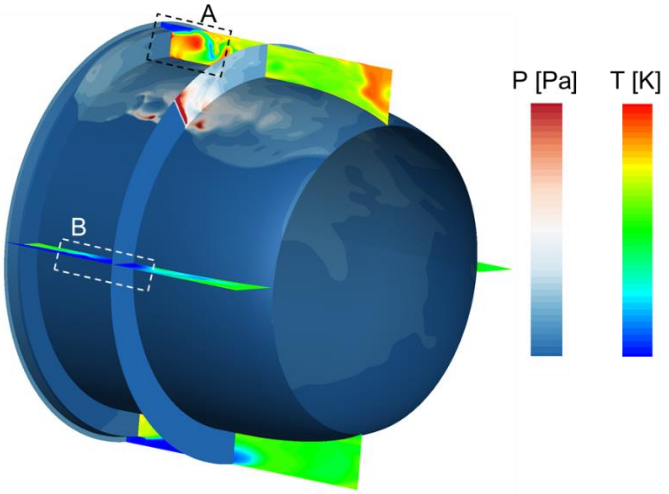

Figure 4 Static flow temperature and surface static pressure flow field within the Turbine High-Pressure Optical RDE

3. THREE-DIMENSIONAL UNSTEADY ANALYSIS OF THE OUTLET PROFILES

3.1. Investigated passages geometries

Figure 5 depicts the investigated geometries, for which the inlet conditions and injection geometry are kept identical. In Figure 5a the diverging geometry is highlighted (installed in the experimental rig of Athmanathan et al. [23], with an outlet-to-inlet area ratio of 1.6, measured downstream of the backward-facing step) while Figure 5b plots a straight passage (outlet-to-inlet area = 1) and Figure 5c a converging-diverging passage. The throat of the latter was designed based on a mass flow averaged Mach number of 1.2 upstream of the throat (expected maximum Mach number in straight RDCs) and decelerate the flow to Mach 0.6 downstream of the throat (outlet-to-inlet area = 1.2).

Table 1 describes the geometries from Figure 5 and indicates in which section of the manuscript the geometry is used, along with its functionality (used as accelerating passage with low back pressure or diffusing passage with elevated back pressure).

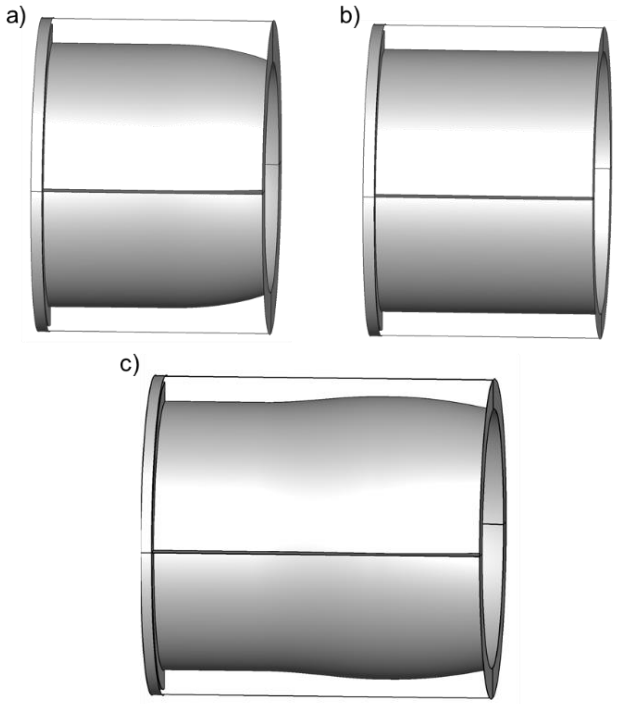

Figure 5 Selected downstream passage geometries: a) diverging geometry, b) straight geometry, c) converging-diverging geometry

Table 1 List of the geometries and their functionality with cross-reference to the specific

name of the geometry	employed as accelerating passage	employed as diffusing passage
Diverging	in 3.2, 4.1, 4.2	in 3.3, 4.1, 4.2
Straight	in 3.2	not analyzed
Converging Diverging	not analyzed	in 3.3, 4.1,4.2,4.3

3.2. Characterization of the accelerating passage with a back pressure of one bar

This section describes the phenomena occurring in accelerating passages required for supersonic axial, radial, or bladeless turbine designs, accomplished by adopting a back pressure of one bar at the outlet of the RDC. In Figure 6a, the radial mass flow averaged outlet Mach number across the spanwise location (θ) is calculated for a high inlet mass flow (inlet total pressure of 10 bar) to achieve the required pressure ratio for the supersonic outlet. The results indicate that for high mass flows, the desired supersonic exit conditions for the diverging geometry (solid lines) are indeed achieved, with a mass flow averaged Mach number at the exit of around 1.65. In contrast, the straight geometry (dashed lines) remains transonic with a mass flow averaged value of about 0.96. Tangentially downstream of the oblique shock (Figure 6b), flow angles of 20 degrees are present, and in the low momentum region the flow angles decrease to -20 degrees. The local total enthalpy ($\dot{m}H_{total}$), (Figure 6c) indicates that peak enthalpy resides tangentially downstream of the rotating shock. The diverging passage features two detonation

waves and is visualized by two high enthalpy regions. The red line depicts the mass-flow averaged total enthalpy ($\dot{m}H_{total}$) and 50% of the flow's total energy is contained within 25% of the circumference.
Figure 6d depicts the mass flow averaged total pressure across the axial length. At the outlet of the accelerating passage, the total pressure loss is around 45%. A first pressure loss occurs through the injection (about 20%), followed by a constant region in which combustion occurs (~z=0.055m) and ultimately, losses due to the acceleration of the flow (around 15%).

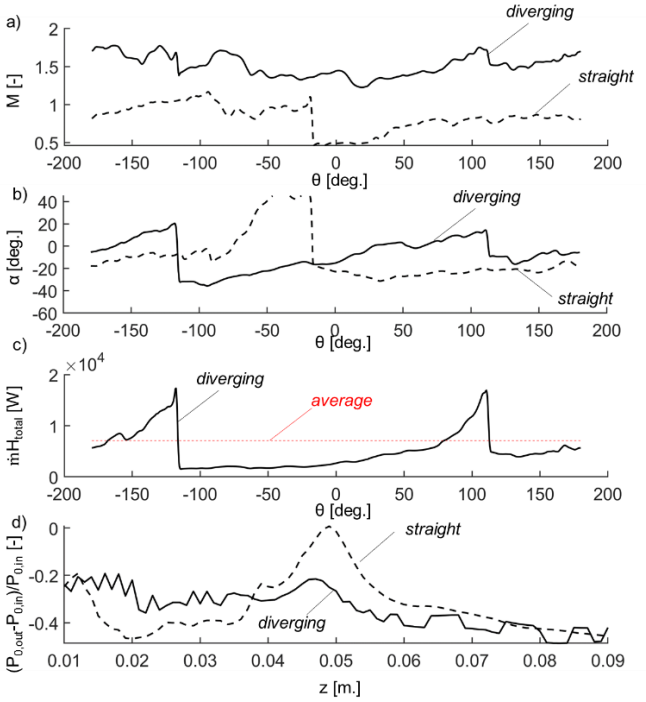

Figure 6 Radially mass flow averaged outlet conditions as a function of the circumference for the low back pressure (one bar) for straight and diverging geometry at highest mass flow (1.2 kg/s): a) Mach number, b) $\dot{m}H_{total}$ c) flow angle and d) mass flow averaged pressure drop as a function of the axial distance

Table 2 summarizes the mass flow averaged values and standard deviation required to model an accelerating passage as inlet conditions to a supersonic turbine configuration by quantifying the Mach number, flow angle, as well as static pressure, and static temperature. The standard deviation in pressure fluctuations (defined in Appendix A1) is around 50% relative to the mass flow averaged static pressure, while this is about 13% for the static temperature.

Figure 7a represents the mass-flow averaged Mach number across the passage as well as the maximum and minimum Mach numbers at each axial location. At a distance of 0.05m, near the onset of the diverging section, acceleration occurs. Minimum Mach numbers, located in the low momentum region, are transonic. Figure 7b plots the flow angles, whereas mean mass flow averaged flow angles are around zero. The maximum flow angles, found in the high momentum region tangentially downstream of the shock, decrease to around 20 degrees due to the passage's acceleration. Hence, in this passage, the acceleration of the axial flow component is predominant with positive flow angles at a location of z=0.03 due to circumferential recirculating hot products downstream of the backward-facing step with high radial flow distortion.

Table 2 Characteristics of the diverging and straight geometry used as accelerating passage for a low back pressure of one bar (sampled 5 mm upstream of the nozzle outlet)

geometry	$M_{massflow\ av.}$	M_{STD}	$\alpha_{massflow\ av.}$ [deg]	α_{STD} [deg]
Diverging	1.6	~0.17	-2	15
Straight	0.96	~0.2	-3.3	21
	$p_{s,\ std.}/p_{s,\ massflow\ av.}$		$T_{std.}/T_{s,,massflow\ av}$	
Diverging	~50%		~13%	
Straight	~43%		~17%	

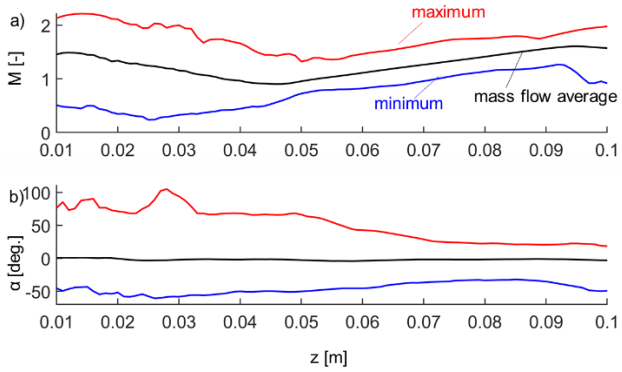

Figure 7 a) Mass-flow averaged, minimum and maximum for the diverging passage as a function of the axial distance of a) Mach number and b) flow angle

A simulation with isothermal wall boundary conditions (in which the walls' temperature was set at 800K) was performed to determine the convective heat flux. The convective heat flux allows for the scaling of heat flux estimates for a range of wall temperatures. Figure 8a plots the instantaneous convective heat flux coefficient ($h = \frac{Q}{T_g - T_{wall}}$) of the unwrapped shroud end wall (a) and hub end wall (b) with a wall temperature of 800K and a gas total temperature of 2300K, corresponding to the mass flow averaged total temperature at the exit of the passage). The detonation wave travels across both end walls in the accelerating passage, with maximum convective heat flux coefficients found tangentially downstream of the detonation wave.
The spanwise-averaged convective heat flux is around 2000 W/K/m^2 with higher values on the hub end wall than the shroud end wall and decreases towards the outlet to 1000 W/K/m^2(Figure 8). The spanwise integrated heat flux coefficient indicates similar hub and shroud values, confirmed by the total heat load, 93 kW for the hub and 99 kW for the shroud.

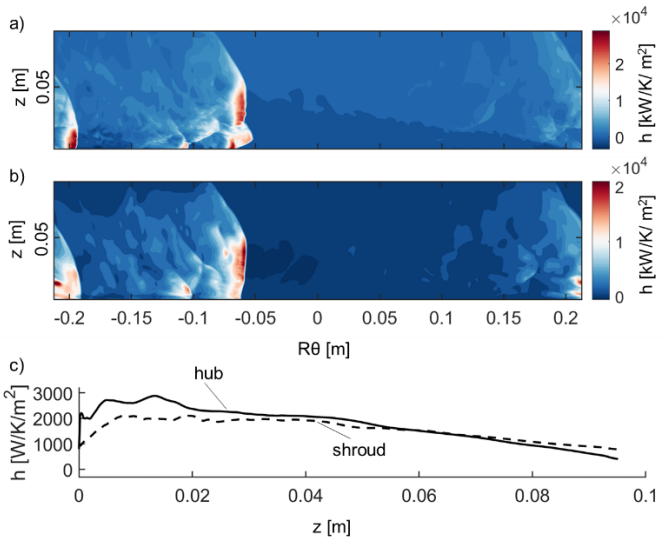

Figure 8 Instantaneous convective heat flux coefficient on the shroud (unwrapped) for the accelerating passage with diverging geometry, b) instantaneous heat flux signature on the hub (unwrapped) for the converging-diverging shape c) Tangentially averaged convective heat flux along the axial direction,

3.3. Characterization of the diffusing passage

In this section, the combustor's outlet pressure is increased to 7 bar to model the downstream turbine's effect/blockage. The selected back pressure was chosen to account for a maximum Mach number of 0.6 at the passage's outlet, suitable for accommodating optimized stator end walls such as those proposed by Liu et al. [17]. Two different passages were investigated. The first one, plotted in Figure 9, is a long passage (length 0.15 m) with a converging-diverging shape. The second one is the baseline, a diverging geometry (Figure 9b). The pressure contour indicates that several reflective shocks occur within the passage (three reflective waves are observed for the converging-diverging diffuser). Furthermore, the detonation region is significantly shortened due to the higher backpressure, and the combustion takes place immediately downstream of the backward-facing step, with all combustion occurring roughly 0.02 m downstream of the backward-facing step extending up to 0.05 m for the accelerating passage. Besides, the converging-diverging geometry features three detonation waves at this condition and during the startup sequence, while the diverging passage supports four detonation waves. Local separation occurred tangentially upstream of the shock in the low momentum region.

Figure 10 plots the relevant outlet quantities, radially mass flow averaged across the span. Figure 10a plots $\dot{m}H_{total}$ highlighting the regions with local highest enthalpy as well as the mass-flow averaged mean. The region tangentially downstream of the shock features low momentum/enthalpy (with local negative values tangentially upstream of the shock).

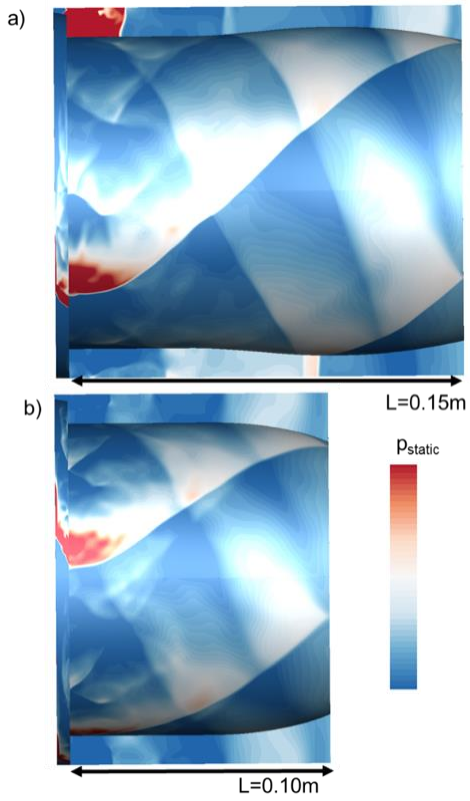

Figure 9 Static pressure flow field of a high back pressured RDC: a) converging-diverging geometry, b) diverging geometry

The converging-diverging geometry has higher averaged energy content (green dashed line) than the diverging part (red dashed line), and both below the accelerating passage. Similar to the accelerating passage, the zone of high enthalpy extends to a span of 50 degrees downstream of the shock. For both cases, 50% of the energy is contained within 33% of the span (denoted by the arrows), slightly higher than the accelerating passage. Figure 10b shows higher peak Mach numbers for the converging-diverging passage (peak Mach numbers of 0.6). Simultaneously, the Mach numbers only reaches 0.4 for the diverging geometry, owing to the more extensive diffusion for the diverging geometry. Mach number is below 0.1 tangentially upstream of the shock, with mainly stagnant swirling flow moving at the oblique shock speed. Figure 10c plots the flow angle at the passage outlet, and significant differences between the two passages are observed. Although maximum flow angles, dictated by the oblique shock, are similar (around 40 degrees), the flow angle decay differs between the two passages, with higher flow angle decay for the diverging passage compared to the converging-diverging passage. In the green-highlighted region, approximately 50 deg. of the span, which contains the highest enthalpy, flow angle variation varied from 30 degrees to -30 degrees for the diverging case, while this only decreased to ~-5 degrees for the converging-diverging passage. In the highest enthalpy region, the total pressure fluctuations reach within 30% (min-to-max) of the mass flow averaged value.

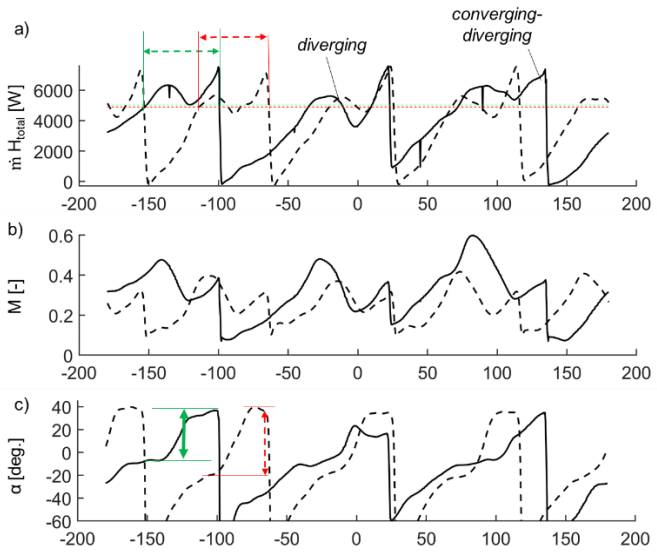

Figure 10 Radially mass flow averaged outlet conditions as a function of the circumference for the diffusing passage (with diverging and converging diverging geometry) at the highest mass flow (1.2 kg/s): a) $\dot{m}H_{total}$, b) Mach number, c), flow angle

In Table 3, the mass-flow averaged quantities of interest to the turbine are tabulated, together with the standard deviations of the fluctuations. The converging-diverging geometry has a mass flow averaged outlet Mach number of ~0.36 (+- 0.13) and the diverging shape M=0.29 (+- 0.08). The fluctuations of pressure and temperature are significantly lower than the accelerating passage. The deviation in the flow angle can be up to 40 deg, however these negative flow angles are located within the downward momentum flow region. Hence, only providing the mean and standard deviation of the outlet fluctuations would not provide all the required information to design the downstream turbine.

Table 3 Mass-flow averaged characteristics with their standard deviation of the diffusing geometry (sampled 10 mm upstream of the diffusing geometry)

geometry	$M_{massflow\ av.}$	M_{STD}	$\alpha_{massflow\ av.}$ [deg]	α_{STD} [deg]
diverging	0.29	~0.08	-1.01	~39
converging-diverging	0.36	~0.13	-1.44	~34
	$p_{0,\ std.}/p_{massflow\ av.}$		$T_{0,\ std.}/T_{massflow\ av}$	
diverging	~22%		~4.7%	
converging-diverging	~22.4%		~4.8%	

Figure 11 describes the change of flow angle (a), Mach number (b), and total pressure (c) across the axial length of the combustor-passage with the mass flow averaged value, local minimum (blue curve), and maximum (red curve) mass flow averaged across the radius for the diverging and converging-diverging geometries ().

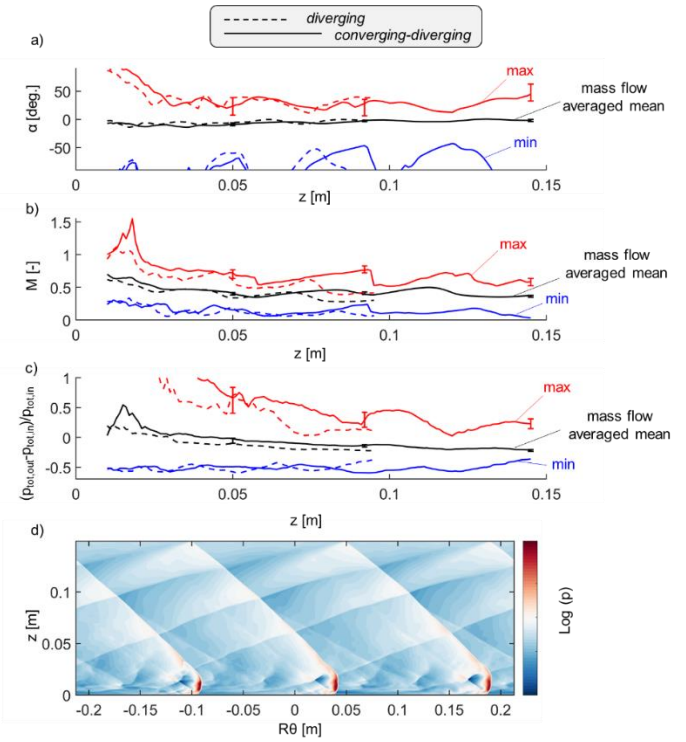

Figure 11 a) Mass-flow averaged, minimum and maximum Mach number as a function of the axial distance, b) flow angle, c) total pressure loss, and d) unwrapped pressure flow field of the diffusing passage with converging-diverging geometry

The maximum flow angle decreases for both passages to about 35 deg. Around the throat region, at 0.1m, the maximum Mach number drops from 0.7 to 0.5; beyond this point, the flow experiences acceleration again. Overall, both passages diffuse the flow as the Mach number decreases over the axial distance. The diverging nozzle reaches a total pressure loss of 20% at the passage exit. Figure 11d depicts the unwrapped converging-diverging combustor-passage, in which several reflecting shock locations are identified, which coincide with local zones of acceleration. The uncertainty bands in Figure 11a,b,c depict the local unsteadiness at that axial location. High variations of maximum Mach number and flow angle, as well as, as well as the pressure tangentially downstream of the oblique shock are observed at a location of 0.05 and upstream of the throat (~0.092 m). The unsteadiness in radially mass-flow averaged quantities near the outlet of the converging-diverging geometry modeled as passage for two detonation cycles is visualized in Figure 12 for the flow angle, Mach number, and total pressure across the perimeter. Local fluctuations in flow angle can vary between 28 and 45 deg., mass flow averaged maximum local outlet pressure losses fluctuates between 0.09 and 0.25. Mass flow averaged pressure across the span remains between 20 and 23%.

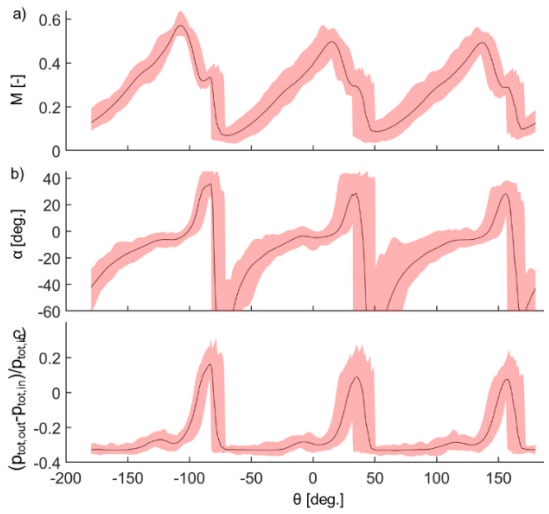

Figure 12 minima and maxima of radially mass-flow averaged quantities around the circumference for two detonation cycles: Mach number (a), flow angle (b), and pressure loss (c) at the outlet of the converging-diverging geometry used as a diffusing passage

Figure 13 depicts the convective heat flux coefficient ($h = \frac{Q}{T_g - T_{wall}}$) of the unwrapped converging-diverging passage with a wall temperature of 800K and a gas temperature of 2200K (mass flow averaged outlet total temperature).

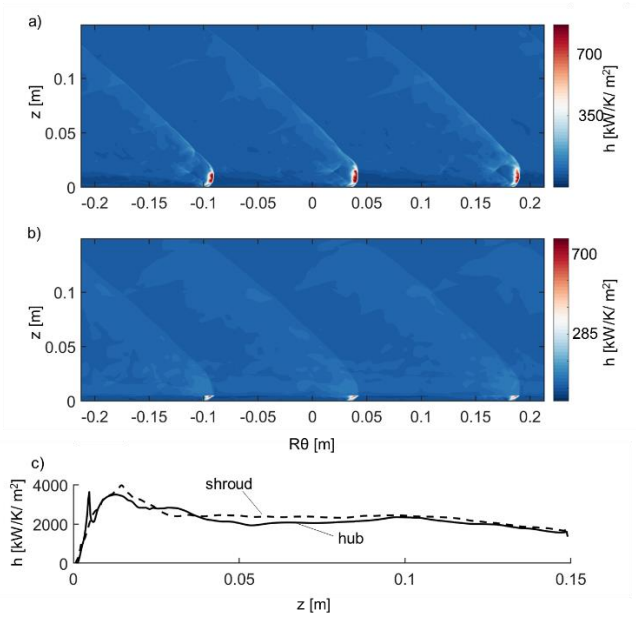

Figure 13 a) Instantaneous convective heat flux coefficient on the shroud (unwrapped), b) instantaneous heat flux signature on the hub (unwrapped) for the converging-diverging shape c) Average convective heat flux for the converging-diverging geometry used as diffusing passage

Maximum heat fluxes are observed within the detonation front for the shroud (Figure 13a) whereas the hub (Figure 13b) features a more constant convective heat flux as the detonation wave rides across the shroud (Figure 13b).

Figure 13c depicts the averaged heat transfer coefficient across the passage for the shroud and hub end wall, with a maximum heat flux coefficient of around 4200 W/m^2/K and decays to about 2900 W/m^2/K near the exit of the passage. The required coolant heat load to keep the end walls at 800K, is around 360 kW. In contrast to the diverging accelerating passage, the convective heat flux coefficient remains constant throughout the passage at about 2000 W/K/m^2 before decreasing downstream of the throat. Additional cooling would be required for longer diffusing passages.

3.4 Operating map

An operating map of the combustor-passage as a function of the mass-flow averaged Mach number, and total pressure loss at the passage's outlet with their respective mass flows is plotted in Figure 14. For low back pressured devices (required for supersonic bladed and bladeless concepts), Mach numbers can reach up to Mach 1.65 for a diverging geometry with a total pressure loss of 55%, whereas a Mach number of 1.2 was achieved for the straight passage. For high back pressured devices, the mass flow averaged Mach number decreases with a consequent reduction in total pressure loss (from 60% to 20%) compared to accelerating passages. Kaemming and Paxson [27] observed similar phenomena in which pressure gain was increased for higher back pressured devices for a fixed injection geometry, due to the lower flow speeds accross the passage.

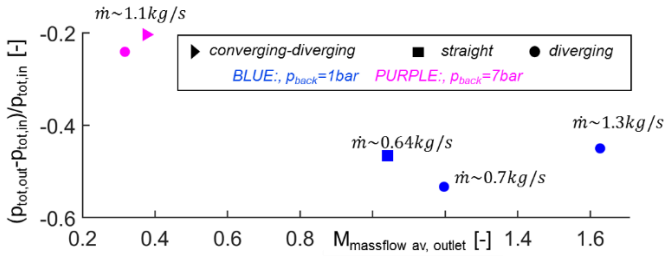

Figure 14 Operating map of all the investigated geometries operating as an accelerating passage (p_{back} = 1bar) and diffusing passage (p_{back} = 7bar) as a function of mass flow averaged Mach number and total pressure drop

4. AERODYNAMIC PASSAGES' PERFORMANCE

4.1. Passage inlet profile defined by the combustor

In Figure 15 the mass flow averaged quantities as a function of the span downstream of the combustion zone were investigated to enable precise modeling of the connecting passage between combustor and turbine. That location was determined based on the maximum total temperature, which occurred at 0.025m for the diverging diffuser, 0.03m for the converging-diverging diffuser, and 0.065m for the diverging nozzle.

Due to the higher expansion occurring in the accelerating passage, a lower total pressure plateau is reached; however, peak total pressures for the three passages are similar (around 20 bar). Higher maximum total temperatures are achieved for the accelerating profile, compared to the two diffusing passages

(Figure 15), which could be attributed to the difference in static temperature upstream of the combust (averaged injection speeds is around Mach 1 ~ 240K). For the accelerating passage a Mach value of 1.7 and temperature of 180K are observed. The Mach number (Figure 15c) is also is significantly higher for the accelerating passage, indicating that the combustion process occurs at high flow speeds. From the total enthalpy ($\dot{m}\, H_{total}$, Figure 15e), 50% of the flow enthalpy lies within 31% of the span for the diffusing passage (similar to the exhaust profile).

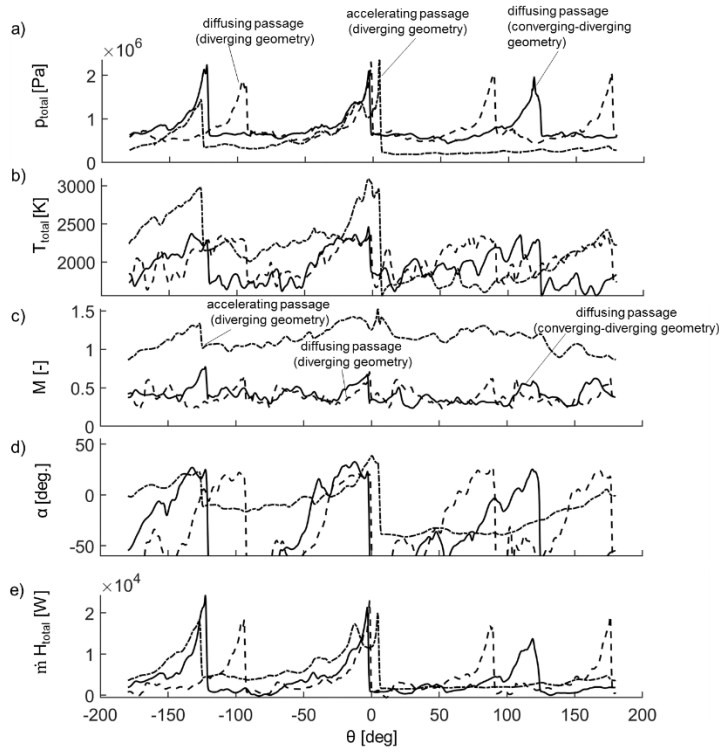

Figure 15 Radially mass-flow averaged profiles downstream of the combustion region for the three passages, a) total pressure, b) total temperature, c) Mach number, d) flow angle, e) $\dot{m}\, H_{total}$

In comparison, this is 22% for the accelerating passage. The maximum flow angle (Figure 15d) for the accelerating passage is found to be between 20 and 30 degrees.

Table 4 Mass flow averaged inlet characteristics and total enthalpy at the onset of the accelerating and diffusing passage

	M [-]	α [deg]	p_0 [bar]	T_0[K]	$\dot{m}\, H_{total}$ [MW]
accelerating passage (diverging)	1.17	-3.2	6.3	2300	5.13
diffuser (diverging)	0.44	-6.9	10.4	2130	3.71
diffuser (converging-diverging)	0.47	-9.14	10.6	2070	3.97

The converging-diverging diffuser's flow angle profile can significantly vary over the axial length (Figure 10c), exhibiting a significant reduction in the flow angle range at the exhaust. Table 4 shows the mass flow averaged values sampled downstream of the combustion region. The accelerating passage features the highest total enthalpy (computed with an averaged specific heat, c_p, 1700 J/kgK) compared to the diffusing passages (between 3.7 and 3.9MW).

4.2. Passage pressure loss

The total pressure drop attributed to the acceleration or diffusion is investigated by isolating the passage downstream of the combustion zone (0.025m for the diverging diffuser, 0.03m for the converging-diverging diffuser, and 0.065m for the accelerating passage), as sketched in Figure 16a. The total pressured drop across the accelerating passage is around 13%, and this pressure drop is dependent on the oblique shock strength and rotational speed. Figure 16b plots the pressure drop as a function of axial length for the isolated passage with similar total pressure drops for the two diffusers but with a different decay due to the difference in length and curvature. The pressure drop for the converging-diverging diffuser is around 25%. Table 4 summarizes the losses of the respective passages as well as the number of detonation waves.

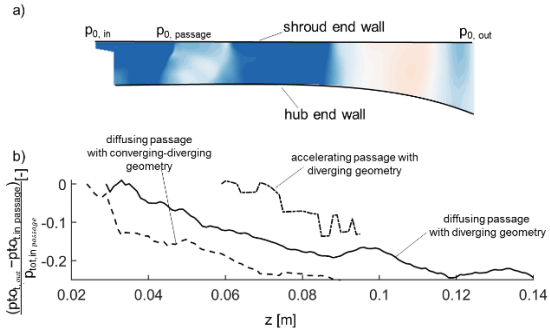

Figure 16 a) Cross-section of the combustor-passage, and b) mass flow averaged total pressure loss of three isolated geometry (an accelerating passage with diverging geometry, diffusing passage with converging-diverging geometry, and the diffusing passage with diverging geometry)

Table 5 Summary of the pressure losses for the isolated passages

	accelerating passage (diverging geometry)	diffusing passage (diverging geometry)	diffusing passage (converging-diverging geometry)
Detonation waves	2	4	3
Passage without combustion	0.04	0.12	0.075
Pressure loss across the passage	13%	24.4%	25%

4.3 Simulation of the isolated diffusing passage

Modeling of isolated accelerating passages for RDCs has already been discussed in [28]. Schwer employed a similar method for modeling the plenum upstream of the RDC [9] and Rankin et al. modeled a converging-diverging nozzle for the RDC to reduce the periodic fluctuations [29]. Hence, the focus lies on accurately modeling the diffuser. The total pressure, total temperature, and velocity direction (flow angles) downstream of the combustion region of the reactive simulations are then imposed as a total pressure and temperature profile with direction profile (unsteady in time and space) in a non-reactive unsteady three-dimensional simulation. This non-reactive simulation (with ~6 million grid points) has a calculation time of around 48 hours on two High-Performance nodes compared to the coupled simulations, which require about 500 hours on six High-Performance nodes. The contours of Figure 17 represent the axial (a) and tangential (b) velocity signature at the inlet interpolated on a 27 (radial) by 1200 grid. This fine interpolation allows rebuilding the combustor outlet profile accurately.

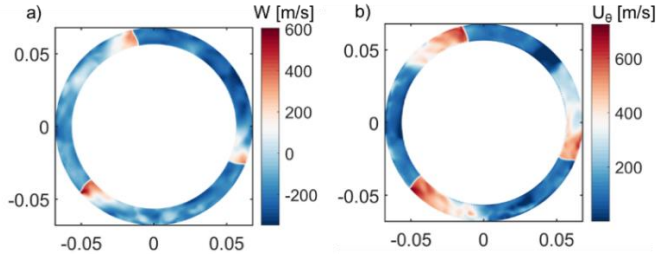

Figure 17 Contour of the interpolated inlet conditions to the diffuser: a) axial velocity and b) tangential velocity

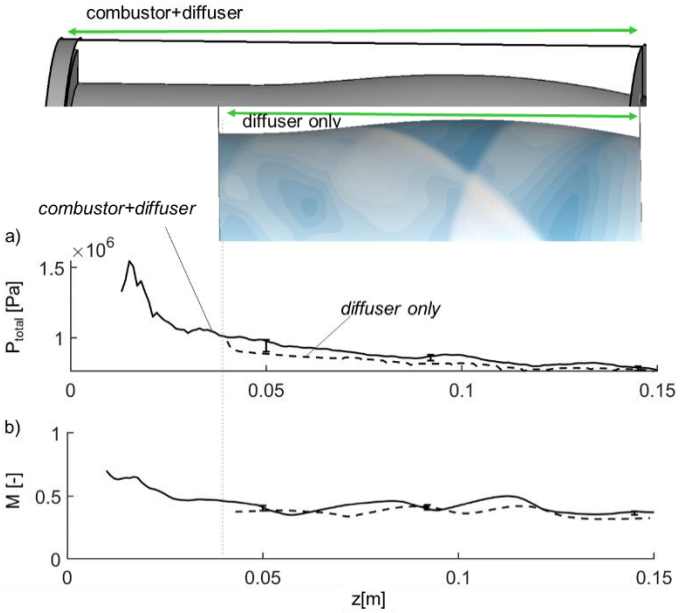

Figure 18 Verification of the diffusing passage-only simulation vs. the 3D URANS with chemistry for the converging-diverging geometry: a) mass-flow averaged pressure drop across the channel, b) mass-flow averaged Mach number along the axial length

The mass flow averaged total pressure is calculated at each axial location. A 25% of mass flow averaged total pressure decrease was measured throughout the reactive simulation's diffuser part, comparable to the simulations with combustion and diffusing passage (Figure 18a). Additionally, the temporal evolution at three distinct axial locations from the 3D URANS with chemistry was added, indicating that the diffusing passage only simulations (with converging-diverging geometry) are within 2% of the combustor-diffuser simulations. The mass-flow averaged Mach number (Figure 18b) at the diffuser outlet decreased from 0.37 to 0.32, and although local variations occur in the diffuser-only simulations, the outlet conditions were matched.

5. CONCLUSION

This paper proposes a novel strategy to assess the performance of high-speed transition elements. Such a procedure, independent of the actual combustor geometry, provides the procedure to assess loss and heat flux at the end walls. The analysis of the various families of transition elements provide guidelines for future designers. Specifically, accelerating and diffusing passages for rotating detonation combustors are characterized through three-dimensional unsteady Reynolds Averaged Navier Stokes (URANS) simulations for a stoichiometric hydrogen-air mixture with a one-step reaction mechanism. First, a validation of the numerical tool was performed and confirmed the ability to capture the major physical phenomena from MHz chemiluminescence and OH PLIF imaging. The relevant quantities for the aero-thermal design of the turbine (flow angle, Mach number, total pressure, and total temperature), as well as passage cooling requirements (through time-resolved convective heat flux), are studied in detail for several passage geometries and a fixed injector from Purdue's Turbine High-Pressure Optical RDC. We observed that the combustion was significantly altered by the combustor pressure ratio. At low back pressures, resulting in accelerating passage for diverging geometries, the combustion zone covered 60% of the passage length, and complete supersonic flow across the span was achieved. The combustion zone was reduced to 20% for the diffusing passage with higher backpressure, and mass-flow averaged Mach numbers of around 0.32 were obtained. The profiles for two different diffusing passages were investigated, a diverging and converging-diverging passage. Significant changes were observed concerning the peak Mach numbers and flow angle variation in the flow's high enthalpy region. The total pressure drop throughout the isolated diffuser was 25%, while this was around 13% for the nozzle. The pressure drop across the injector and combustion zone was higher for the accelerating passage, resulting in an overall more considerable total pressure drop but higher total enthalpies for the accelerating passage. Total pressure, total temperature, and flow angle profile at the exit of the combustor for the two diffusing passages with same combustor inlet-to-outlet pressure ratio shared similar features. Hence, the isolated diffusing passage was modeled, and similar mass flow averaged total pressures signature across the axial length was obtained, with a tenfold reduction in computational time.

6. ACKNOWLEDGMENTS

The authors would like to acknowledge the U.S. Department of Energy for the part-time faculty appointment of Prof. Paniagua to the Faculty Research Participation Program at the National Energy Technology Laboratory and the support of James Braun in part by appointment to the National Energy Technology Laboratory Research Participation Program, sponsored by the U.S. Department of Energy and administered by the Oak Ridge Institute for Science and Education. The authors would like to thank Prof. Terrence Meyer and Venkat Athmanathan for the discussion with the experimental results. Finally the authors would like to thank Metacomp for their help.

7. APPENDIX

A1. Quantities of interest

The quantities of interest are defined as follows: time-averaging of mass flow averaged quantities is performed according to Equation 1. First, a spatial mass flow averaged value is computed, which is then time-averaged.

$$M_{mass\ flow\ av.} = \int \frac{\int M.u_{axial}.\rho\, dA}{\int u_{axial}.\rho\, dA} dt/\Delta t \qquad \text{(Eq. 1)}$$

Circumferential flow angles are defined as

$$\alpha = \tan\left(\frac{u_{tangential}}{u_{axial}}\right) \qquad \text{(Eq. 2)}$$

And total pressure loss is computed according to the mass-flow averaged value,

$$\text{Pressure loss} = \frac{\frac{\int p_{total,out}.u_{axial}.\rho\, dA}{\int u_{axial}.\rho\, dA} dt}{\frac{\Delta t}{p_{total,in}}} - p_{total,in} \qquad \text{(Eq. 3)}$$

Standard deviations of a quantity X are determined according to Equation 4, with N the total amount of samples.

$$X_{STD} = \sqrt{\frac{1}{N-1}\sum_{i=1}^{N}\left|X_i - X_{mass\ flow\ av.}\right|^2} \qquad \text{(Eq. 4)}$$

A2. Convergence

To reduce simulation time, an inviscid simulation with no boundary layer refinement was initiated and afterwards interpolated to a viscous mesh to obtain the viscous solution. The information of the last seven detonation cycles of the RDC is visualized in Figure 19. The mass-flow averaged Mach number at the outlet is around 1.2 (black curve, Figure 19a). The total pressure loss at the combustor outlet is about 52% (blue curve Figure 19a), mostly attributed to the existence of the backward-facing step, which creates large pressure losses. Figure 19b depicts the last eight cycles of the Mach number and shows the Mach number's convergence. To ensure convergence, approximately ten cycles of the viscous simulations are modeled. Figure 19b depicts the Mach number at the combustor's exit for three different radial positions. A cyclic event is obtained with Mach numbers up to 1.5 tangentially downstream of the oblique shock. For both criteria, convergence is observed after seven cycles requiring computational time of 600 hours on six 20-intel cores.

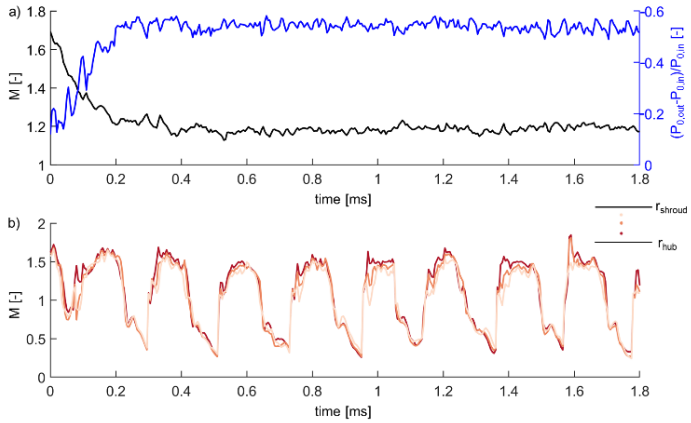

Figure 19 a) Total pressure loss and mass flow averaged Mach number as a function of time, b) Mach number at three radial locations for the last seven cycles as a function of time for eight cycles

A3. Premixed vs non-premixed simulation

To better understand the implications of the premixed simulation, shown in Figure 20b, on the RDC's outlet condition, and a non-premixed combustor (Figure 20c), the outlet profiles were compared to a premixed simulation. The Mach number outlet profile at mid-radius for both profiles is given Figure 20a, with the dashed lines indicating the non-premixed simulations. In contrast, the solid lines indicate the premixed simulations. For a mass flow of 0.7 kg/s, the mass-flow averaged Mach number is 1.17 for the premixed and 1.14 for the non-premixed case. Due to the backpressure (one bar), which was insufficient to maintain supersonic flow across the entire perimeter of the circumference, local zones of subsonic flow (reaching values below Mach 0.5) are observed. Comparable outlet conditions are found and the discrepancy of the mid-radius fluctuations (measured by the standard deviation) between the premixed and non-premixed simulations is below 4%. Therefore, premixed computations with a lower computational burden were utilized to compare the performance of several geometries. Figure 20b and c visualize the flow field of the premixed and non-premixed combustor in which distinct local flow features appear at the combustion zone due to the effect of mixing.

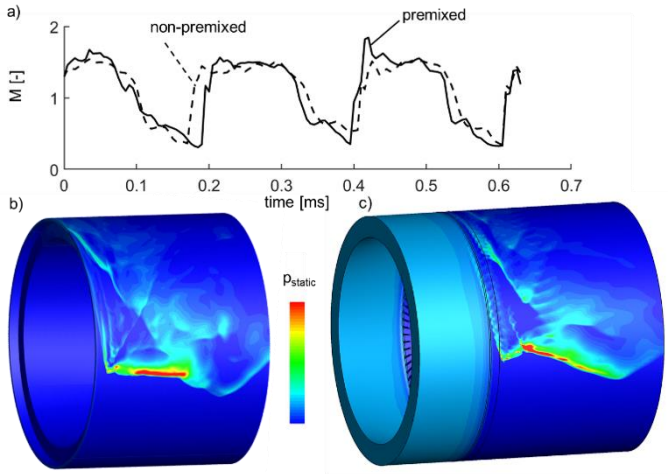

Figure 20 a) Mach number at the exit of the combustor for two cycles for a premixed and non-premixed simulation for six radii, b) pressure flow field of the premixed RDC, c) pressure flow field of the non-premixed RDC

A4. Reaction scheme verification

In Figure 21, three different reaction schemes are compared in a one-dimensional detonation tube simulation. The first reaction scheme is a one-step reaction mechanism with 4 species (N2, H2O,), the second one is an eighteen-step with 9 species (Drummond) and the third is a seven-step reaction mechanism with 7 species (H2, O2, H2O, OH, O, H) (Baurle et al., 1994). The multi-step reactions require a tenfold timestep decrease and small mesh size to obtain accurate results. Pressures and temperatures are compared to the Chapman Jouguet condition. All three reaction schemes predict similar CJ speed but the temperature of the one-step reaction overshoots CJ temperature by 7%.

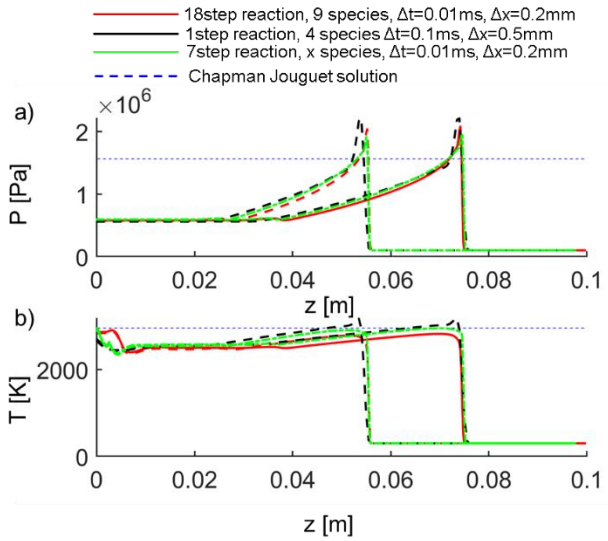

Figure 21 verification of three reaction schemes in a one dimensional detonation tube, 1) static pressure, b) static temperature

A5. Viscous vs non viscous effects

Figure 22 details effects of modeling viscous/inviscid walls, with the inviscid simulations over-predicting the mass flow averaged Mach number at low inlet mass flows, reaching Mach ~1.7. This is approximately 0.4 higher than the viscous calculations. The backpressure is not sufficiently low to keep the supersonic flow, and hence, large portions of the combustor are exposed to subsonic flow. Additionally, the pressure loss for the inviscid simulation is underpredicted by 6% points. The pressure loss is around 53% for lower inlet total pressures and decreases to 45% for the higher inlet total pressures (corresponding to higher inlet mass flows). At higher mass flows, the mass flow averaged Mach number at the combustor's outlet is slightly lower than the inviscid simulation (a ΔM of 0.05) due to blockage from the boundary layer. However, inviscid simulations cannot be used to predict the onset of separation in the diffusing passage nor the convective heat load estimation. Thus, viscous simulations with sufficient wall refinement to accurately model the viscous sublayer in the downstream passage are employed for all geometries being considered in this study.

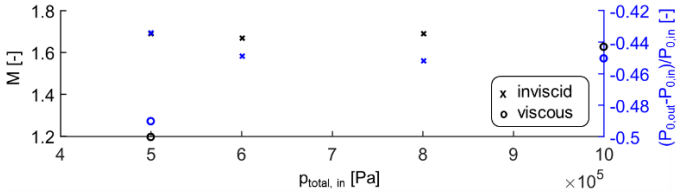

Figure 22 Influence of modeling viscous walls: mass flow averaged Mach number and total pressure drop for an RDC with a diverging nozzle with mixed supersonic/subsonic boundary condition set at one atmosphere

8. REFERENCES

[1] A. Roy, C. R. Bedick, D. H. Ferguson, T. Sidwell, and P. A. Strakey, "Investigating Instabilities in a Rotating Detonation Combustor Operating With Natural Gas–Hydrogen Fuel Blend—Effect of Air Preheat and Annulus Width," *J. Eng. Gas Turbines Power*, vol. 141, no. 11, Nov. 2019.

[2] J. Braun, B. H. Saracoglu, and G. Paniagua, "Unsteady Performance of Rotating Detonation Engines with Different Exhaust Nozzles," *J. Propuls. Power*, vol. 33, no. 1, pp. 121–130, Jan. 2017.

[3] V. Anand and E. Gutmark, "Rotating detonation combustors and their similarities to rocket instabilities," *Prog. Energy Combust. Sci.*, vol. 73, pp. 182–234, Jul. 2019.

[4] J. Z. Ma B. Wang, "Recent Progress, Development Trends, and Consideration of Continuous Detonation Engines," *AIAA J.*, pp. 1–59, Nov. 2020.

[5] D. Schwer and K. Kailasanath, "Numerical investigation of the physics of rotating-detonation-engines," *Proc. Combust. Inst.*, vol. 33, no. 2, pp. 2195–2202, 2011.

[6] S. M. Frolov, A. V. Dubrovskii, and V. S. Ivanov, "Three-dimensional numerical simulation of the operation of a rotating-detonation chamber with separate supply of fuel and oxidizer," *Russ. J. Phys. Chem. B*, vol. 7, no. 1, pp. 35–43, 2013.

[7] P. A. T. Cocks and A. T. Holley, "High Fidelity Simulations of a Non - Premixed Rotating Detonation Engine," no. January, pp. 1–18, 2016.

[8] P. Pal, C. Xu, G. Kumar, S. A. Drennan, B. A. Rankin, and S. Som, "Large-eddy simulations and mode analysis of ethylene/air combustion in a non-premixed rotating detonation engine," *AIAA Propuls. Energy 2020 Forum*, pp. 1–12, 2020.

[9] T. Sato, F. Chacon, L. White, V. Raman, and M. Gamba, "Mixing and detonation structure in a rotating detonation engine with an axial air inlet," *Proc. Combust. Inst.*, vol. 000, pp. 1–8, 2020.

[10] E. Bach, P. Stathopoulos, C. O. Paschereit, and M. D. Bohon, "Performance analysis of a rotating detonation combustor based on stagnation pressure measurements," *Combust. Flame*, vol. 217, pp. 21–36, Jul. 2020.

[11] Z. Liu, J. Braun, and G. Paniagua, "Characterization of a Supersonic Turbine Downstream of a Rotating Detonation Combustor," *J. Eng. Gas Turbines Power*, vol. 141, no. 3, p. 031501, 2018.

[12] J. Braun, G. Paniagua, F. Falempin, and B. Le Naour, "Design and Experimental Assessment of Bladeless Turbines for Axial Inlet Supersonic Flows," *J. Eng. Gas Turbines Power*, vol. 142, no. 4, Apr. 2020.

[13] L. B. Inhestern, J. Braun, G. Paniagua, and J. R. Serrano Cruz, "Design, Optimization, and Analysis of Supersonic Radial Turbines," *J. Eng. Gas Turbines Power*, vol. 142, no. 3, pp. 1–12, Mar. 2020.

[14] M. Asli, P. Stathopoulos, and C. O. Paschereit, "Aerodynamic Investigation of Guide Vane Configurations Downstream a Rotating Detonation Combustor," *J. Eng. Gas Turbines Power*, no. c, Nov. 2020.

[15] Y. Senoo and M. Nishi, "Prediction of Flow Separation in a Diffuser by a Boundary Layer Calculation," *J. Fluids Eng.*, vol. 99, no. 2, pp. 379–386, Jun. 1977.

[16] R. C. Dean and Y. Senoo, "Rotating Wakes in Vaneless Diffusers," *J. Basic Eng.*, vol. 82, no. 3, pp. 563–570, Sep. 1960.

[17] Z. Liu, J. Braun, and G. Paniagua, "Thermal power plant upgrade via a rotating detonation combustor and retrofitted turbine with optimized endwalls," *Int. J. Mech. Sci.*, vol. 188, no. July, p. 105918, Dec. 2020.

[18] C. A. Elmi, F. Agnolio, R. Ferraro, A. Menard, H. Reese, and A. Andreini, "Development of an Integrated Procedure for Combustor Aero-Thermal Preliminary Design," pp. 1–11, 2020.

[19] S. Chakravarthy, O. Peroomian, U. Goldberg, and S. Palaniswamy, "The CFD++ Computational Fluid Dynamics Software Suite," *SAE Tech. Pap. Ser.*, vol. 1, 2010.

[20] D. Fernández-Galisteo, A. L. Sánchez, A. Liñán, and F. A. Williams, "One-step reduced kinetics for lean hydrogen-air deflagration," *Combust. Flame*, vol. 156, no. 5, pp. 985–996, 2009.

[21] J. Saavedra, G. Paniagua, and S. Lavagnoli, "On the transient response of the turbulent boundary layer inception in compressible flows," *J. Fluid Mech.*, vol. 850, pp. 1117–1141, Sep. 2018.

[22] J. Braun, J. Sousa, and G. Paniagua, "Numerical Assessment of the Convective Heat Transfer in Rotating Detonation Combustors Using a Reduced-Order Model," *Appl. Sci.*, vol. 8, no. 6, p. 893, May 2018.

[23] V. Athmanathan J Fisher Z Ayers, J Braun, T Meyer, G Paniagua S. Roy, "Turbine-integrated High-pressure Optical RDE (THOR) for injection and detonation dynamics assessment," in *AIAA Propulsion and Energy 2019 Forum*, 2019, pp. 1–15.

[24] F. Chacon and M. Gamba, "Detonation wave dynamics in a rotating detonation engine," *AIAA Scitech 2019 Forum*, no. January, 2019.

[25] D. P. Stechmann, S. D. Heister, and S. V. Sardeshmukh, "High-Pressure Rotating Detonation Engine Testing and Flameholding Analysis with Hydrogen and Natural Gas," in *55th AIAA Aerospace Sciences Meeting*, 2017, no. January, pp. 1–17.

[26] P. S. Hsu V Athmanathan T Meyer M Slipchenko S. Roy, "Megahertz-rate OH planar laser-induced fluorescence imaging in a rotating detonation combustor," *Opt. Lett.*, vol. 45, no. 20, p. 5776, Oct. 2020.

[27] T. A. Kaemming and D. E. Paxson, "Determining the Pressure Gain of Pressure Gain Combustion," in *2018 Joint Propulsion Conference*, 2018.

[28] J. Braun, J. Saavedra Garcia, and G. Paniagua, "Evaluation of the unsteadiness across nozzles downstream of rotating detonation combustors," in *55th AIAA Aerospace Sciences Meeting*, 2017, no. January, pp. 1–13.

[29] B. A. Rankin, J. Hoke, and F. Schauer, "Periodic Exhaust Flow through a Converging-Diverging Nozzle Downstream of a Rotating Detonation Engine," in *52nd Aerospace Sciences Meeting*, 2014, no. January, pp. 1–12.